

Supplementary Materials:

Intermittence of transient slow slip in the Mexican subduction zone

Zaccaria El Yousfi^a, Mathilde Radiguet^a, Baptiste Rousset^b, Allen Husker^c,
Ekaterina Kazachkina^d, Vladimir Kostoglodov^d

^a Univ. Grenoble Alpes, Univ. Savoie Mont Blanc, CNRS, IRD, Univ. Gustave Eiffel, ISTerre, , Grenoble, 38000, France

^b Institut Terre et Environnement de Strasbourg, Universite de Strasbourg (UMR 7063), , Strasbourg, 67000, France

^c Seismological Laboratory, California Institute of Technology, Pasadena, 91125, California, USA

^d Instituto de Geofisica, Universidad Nacional Autónoma de México, Circuito de la, Investigacion Cientifica s/n, C.U., Coyoacan, 04150, CDMX, Mexico

1 Supplementary methods

1.1 GNSS processing

The GNSS displacement time series were computed using the GAMIT/GLOBK software, which uses a double-difference processing that reduces satellite clock and orbit errors, localized atmospheric errors, and cancels the effects of variations in the receiver clocks. The software incorporates final IGS (International GNSS Service) combination solutions for orbits (with accuracies of 1–2 cm) and Earth Orientation Parameters (EOP). Ionospheric and atmospheric corrections were applied during the processing. Hydrostatic and water vapor delay are corrected using Vienna Mapping Functions (VMF). Solid Earth tide model (IERS03), ocean tidal loading (FES2004), tables for earth rotation values (nutation IAU2000, polar motion, universal time), and precession constant IAU76 are applied. The resulting GPS time series are calculated in the ITRF 2014 reference frame and then rotated with respect to the fixed North American plate using the rotation pole.

1.2 Trajectory model

In the trajectory model from Marill et al. (2021), the daily GNSS time series is fit using a set of base functions representing tectonic and non-tectonic contributions to surface displacements, and the amplitude of each term is estimated using a least squares inversion. The model coefficients are estimated independently for each time series and are defined as:

$$x(t) = v(t - t_R) + \sum_{j=1}^{n_J} c_j H(t - t_j) + \sum_{i=1}^{n_I} m_i H(t - t_i) * \log \left(1 + \frac{t - t_i}{T_R} \right) \\ s + \sum_{s=1}^{n_S} d_s \left(-\frac{1}{2} \cos \left(\pi \frac{t - t_s}{t_d} \right) + \frac{1}{2} \right) + \sum_{k=1}^2 [s_k \sin(2k\pi(t - t_R)) + c_k \cos(2k\pi(t - t_R))] + \sum_{a=1}^{n_A} b_a H(t - t_a) \quad (\text{ES1})$$

where the inverted amplitude terms are:

- v , the linear inter-seismic trend
- c_j , the co-seismic jumps for the n_J considered earthquakes, and $H(t - t_j)$ is a Heaviside function with onset at t_j .

- m_i , the post-seismic transients, for the n_I events with post-seismic slip that starts at the time t_i . T_R is a time constant fixed to 10 days in our study.
- d_s , the long-term SSEs, starting at the time t_s and lasting for a duration of t_d .
- s_k and c_k , the seasonal variations, are defined for annual and semi-annual components.
- b_a , the antenna jumps.

Earthquakes of magnitudes $M_w \leq 6.4$, are neglected in this model, as their surface displacement is not large enough to be seen by GNSS. All other earthquakes are modeled in GNSS time series based on the presence of the station in the impact radius of earthquakes r_{EQ} , which is empirically defined as a function of the moment magnitude: $r_{EQ} = \frac{1}{2.7} 10^{(0.415*M_w - 0.8)}$, with magnitudes and hypocenter coordinates issued by the SSN (Servicio Sismológico Nacional, UNAM). Post-seismic transients are modeled for earthquakes with $M_w \geq 7.2$. The L-SSE periods are based on published studies, and adjusted to best fit GNSS time series (Tables S2 and S3 for Guerrero and Oaxaca regions respectively) (e.g. [Lowry et al., 2001](#); [Radiguet et al., 2011](#); [Graham et al., 2016](#); [Cruz-Atienza et al., 2021](#)).

The longer-term modeled parameters are well estimated and corrected in the trajectory model, particularly the inter-seismic loading trends, and the seasonal variations. Co-seismic and antenna jumps are also well modeled and estimated by the trajectory model using Heaviside functions. Post-seismic and L-SSEs are episodic events that are however less well constrained, as regularly occur at the same time and complicated their independent estimation using similar decaying functions. The period of these modeled events does not affect the ~ 10 days-long signals aimed by this work. A sequence of two L-SSEs occurred in Oaxaca in 2017 and 2018, along with the M_w 8.2 Tehuantepec and 7.2 Pinotepa earthquakes and the associated postseismic deformation [Cruz-Atienza et al. \(2021\)](#). Due to the complexity of the deformation signals during this time period, and the difficulty to separate the different sources of deformations involved, we do not consider the decompositions of the two L-SSEs in 2017 and 2018 in Oaxaca in this work to avoid any artificial signal due to mismodelled afterslip in particular.

1.3 Inversion procedure

The surface slip velocities for the three components, and their associated uncertainties are inverted for fault slip displacements using a least squares formalism similar to [Radiguet et al. \(2011, 2016\)](#).

The cost function minimized in the inversion is:

$$S(m) = \frac{1}{2}[(Gm - d)^t C_d^{-1}(Gm - d) + (m - m_0)^t C_m^{-1}(m - m_0)] \quad (\text{ES2})$$

where d is the data vector containing surface rates, m contains the model parameters (slip increments at each modeled fault patch), and G is the Green's function matrix, computed using Okada's formulation for an elastic half-space (Okada, 1985). C_d , the data covariance matrix, is a diagonal matrix with the data variances, estimated from the one-sigma standard deviations on the random decompositions (Fig. 3.C-D). The model covariance matrix is used to introduce a correlation between fault patches, with the following relation:

$$C_m(i, j) = \left(\sigma_m \frac{\lambda_0}{\lambda} \right)^2 \exp \left(-\frac{s(i, j)}{\lambda} \right) \quad (\text{ES3})$$

where s is the distance between two fault patches, λ_0 is a constant reference correlation length equal to 16.5km, and λ is the correlation length (used as a regularization parameter). σ_m is the standard deviation on the model parameters, used here as a damping parameter.

The model is computed using the linear least-square formulation from Tarantola (2005), and is given by:

$$m = m_0 + C_m G^t (G C_m G^t + C_d)^{-1} (d - Gm) \quad (\text{ES4})$$

where m_0 is the prior model, corresponding in this study to a null slip rate on all patches.

The resolution matrix is given by:

$$R = C_m G^t (G C_m G^t + C_d)^{-1} G \quad (\text{ES5})$$

and the restitution index R_{rest} , is calculated as the sum of the rows is computed for each patch j as $R_{rest}(j) = \sum_i R_{ij}$. This index infers that the local mean value of slip is correctly retrieved by the inversion in the areas of interest.

The regularization is selected as the best compromise between the fit to the data and the model complexity, through L curves (Figure S4). The data misfit is evaluated via the reduced Chi-squares, defined as: $\chi^2 = \sum (\frac{Gm-d}{\sigma})^2$, and the model complexity through the L_2 norm on the slip.

We have performed inversion for 3 different correlation lengths ($\lambda = 20, 50$ and 100 km , Figure S3), and multiple values of a damping coefficient σ_m , though several values of its logarithm $\log_{10}(\sigma_m) = [-3, \dots, 0.5]$, and verified how the evolution of these parameters affected the global misfit between the

observations and the predicted displacement rates. The selected optimal regularization parameters, are $\log_{10}(\sigma_m) = -1.2$ and $\lambda = 50 \text{ km}$ ([Figure S4](#)).

We used this damping coefficient homogeneously for all slip patches, and for all the inversions, except to test the occurrence of S-SSEs without shallow slip. We set a damping variation limit z_{lim} , above which the damping parameter $\log_{10}(\sigma_m)$ is divided by 200, to penalize slip at depths shallower than z_{lim} ([Figure S5](#)).

The slip direction is fixed during the inversion. We impose the orientation of a regional tectonic vector, oriented in the convergence direction (28° North), and then project this horizontal vector on each fault patch to estimate the local rake.

2 Supplementary Figures

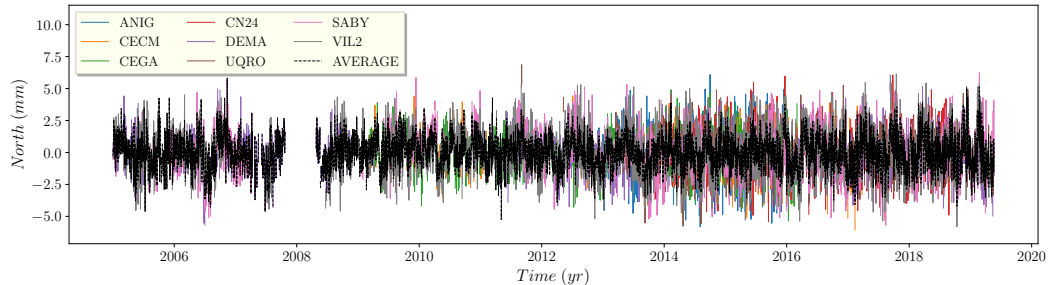


Figure S1: Common mode time series. The colored time series are the residuals of the trajectory model for the GNSS stations shown in the legend. The dashed black line is the average of the 8 residual time series.

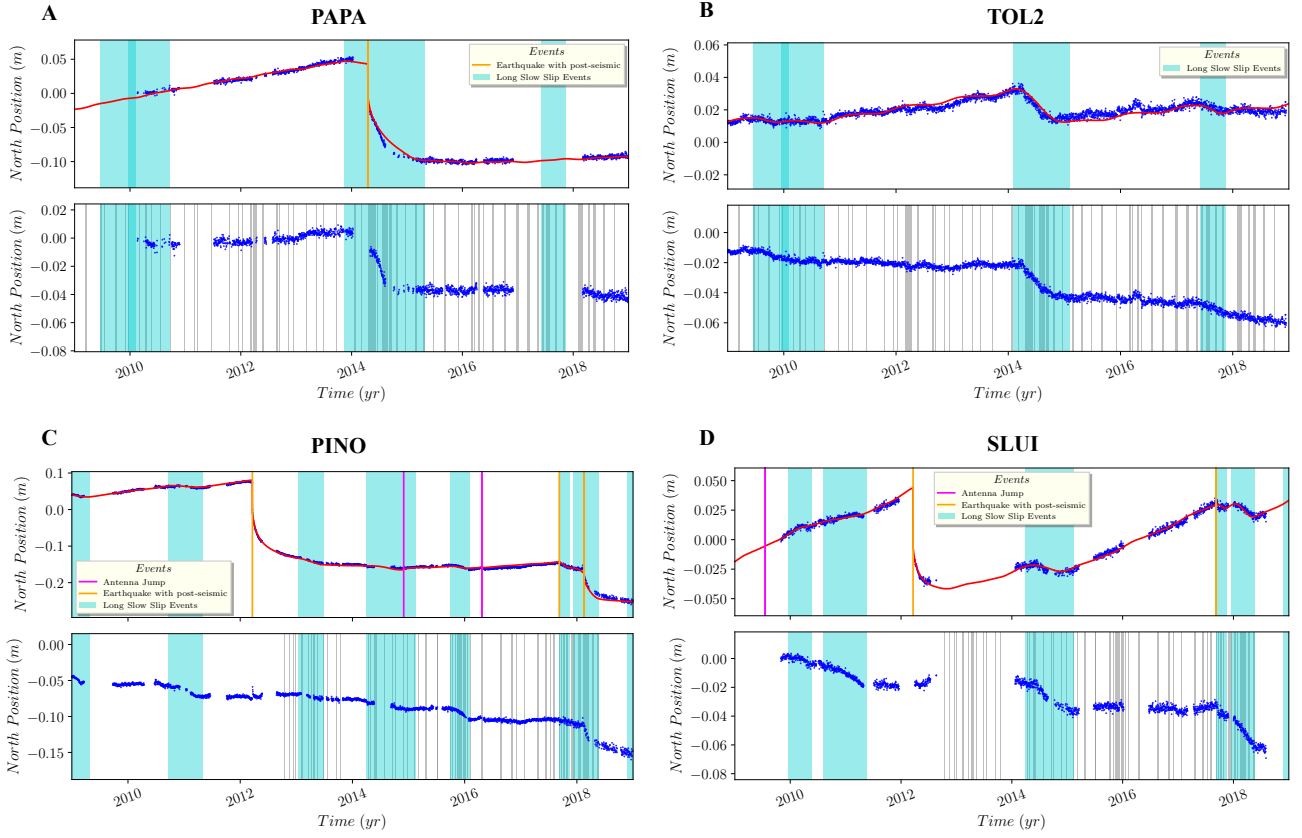


Figure S2: GNSS data and corresponding trajectory models before and after correction. **A** and **B** are the GNSS positions for the stations PAPA and TOL2 in the Guerrero region, and **C** and **D** are the GNSS positions for the stations PINO and SLUI in the Oaxaca region. For each station, the top panel shows GNSS positions in the North direction by the blue dots, the red line is the corresponding trajectory model, and the vertical lines correspond to earthquakes with post-seismic relaxation in orange, and antenna jumps in magenta. Light blue spans correspond to L-SSE periods. The bottom part of each sub-figure shows again the GNSS time series with blue dots, corrected from the linear interseismic trend, co-seismic offsets, post-seismic relaxation, and annual and semi-annual oscillations. On top of the time series, the grey spans show the bursts of tremor.

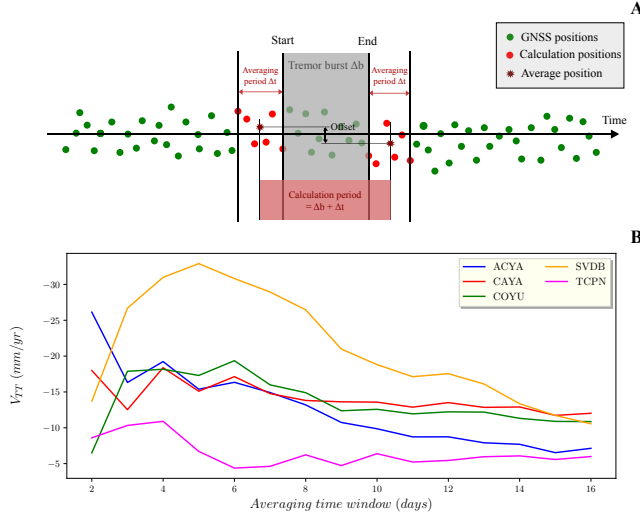


Figure S3: GNSS displacement calculation method by averaging around tremor periods. The top figure (**A**) is a scheme of a GNSS time series (green/red dots), on top of which a gray span shows a tremor period Δb . The red span covers the calculation period, which includes tremor burst duration Δb and the size of the averaging window Δt . The two vertical black lines delimit the averaging periods of the GNSS positions, the averaged positions are shown by red dots, and the average positions are shown with dark red stars. The bottom figures (**B**) show the surface rates during TT periods obtained by the decomposition of the Northern component of GNSS according to tremor burst times. Surface rates have been estimated for different averaging periods to compute the static offsets (as in the top figure). Short averaging periods (< 6 days) show very unstable decompositions results resulting from noisy GNSS time series, and long (> 10 days) averaging periods tend to reduce the velocities by smoothing. The optimal averaging period selected in this study is 6 days. The GNSS sites shown are located close to the coast in the Guerrero region.

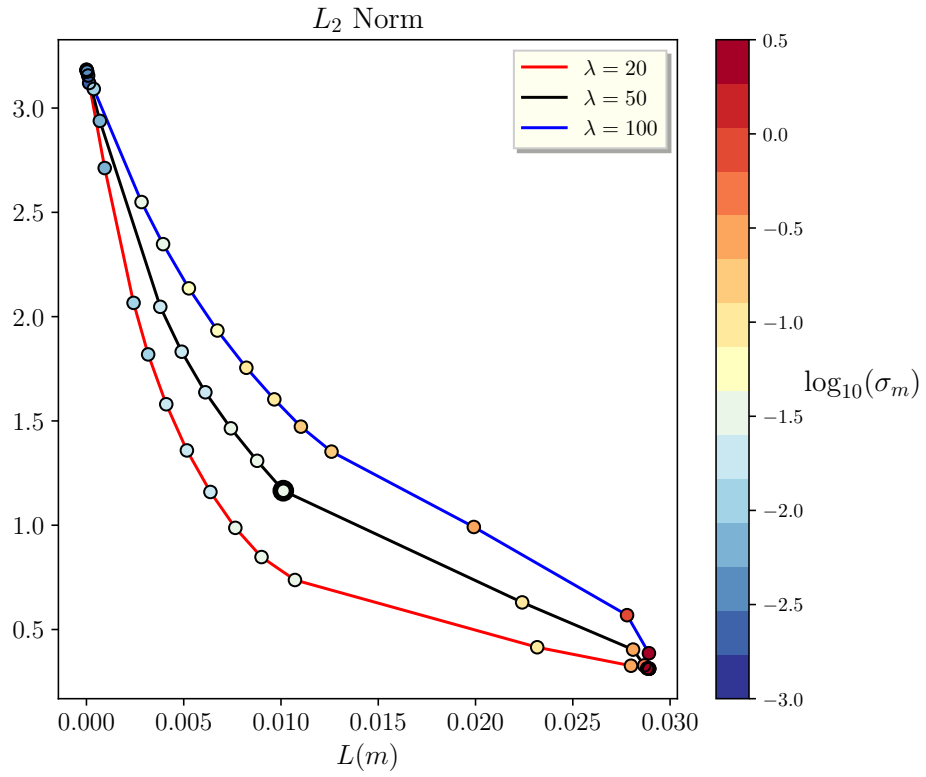


Figure S4: Selection of the regularization parameters through L-curves. The data misfit (Chi-square χ^2) is plotted as a function of the size of the regularized solution (L₂ norm) for different damping values $\log_{10}(\sigma_m)$. The red, black, and blue lines correspond to L curves for correlation lengths λ of 20 km, 50 km, and 100 km respectively. The selected optimal regularization parameters (thick black circle) are $\log_{10}(\sigma_m) = -1.2$ and $\lambda = 50 \text{ km}$. These results correspond to the inversion for S-SSEs in Guerrero (Fig. 5.A).

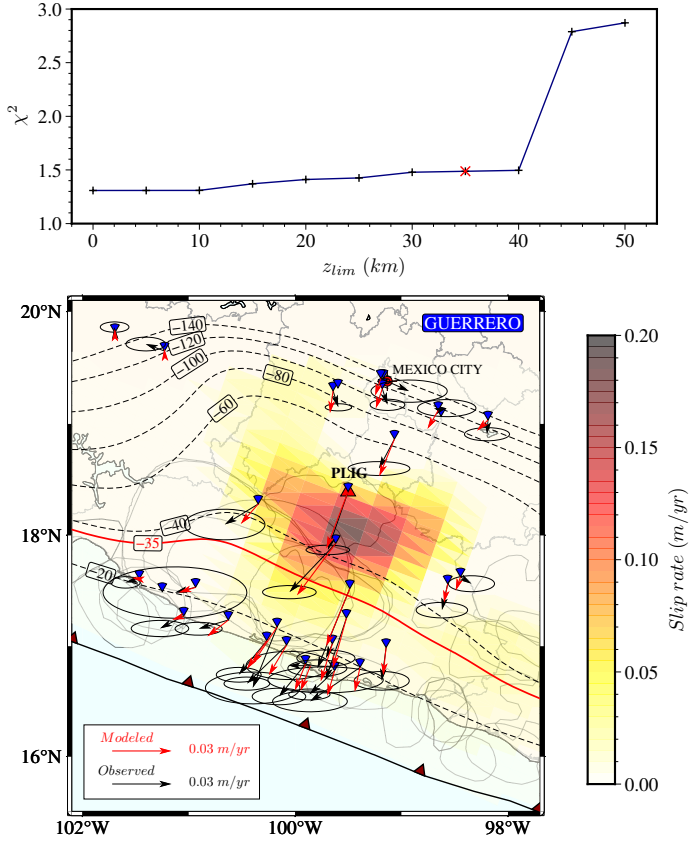


Figure S5: Inversion with penalization of shallow slip. **A** Misfit as a function of z_{limit} , the upper depth limit of slip, for z_{limit} values between 0 and 50km deep. **B** Slip rate map of S-SSEs in Guerrero for $z_{limit} = 35$ km, z_{limit} is shown by the thick red line. The black vectors show the surface rates with 1σ uncertainty, the red vectors are the modeled surface rates, and the colorbar shows the slip rate amplitudes.

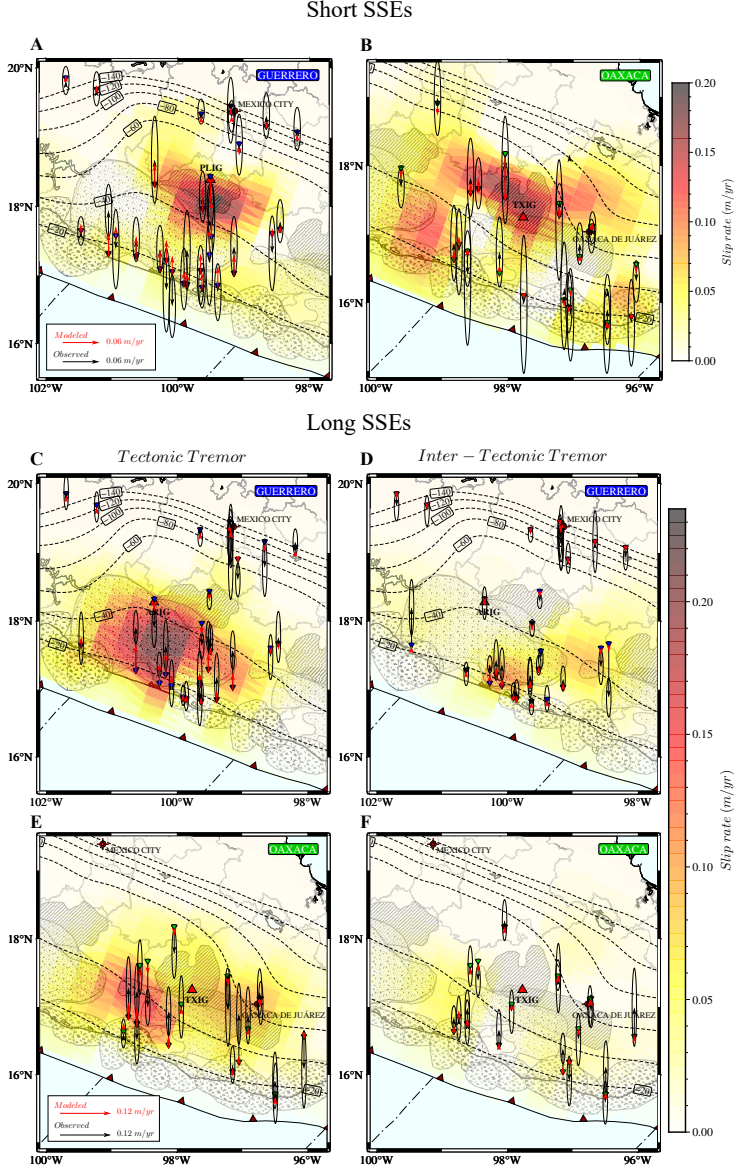


Figure S6: The top maps (**A**, and **B**) displays the vertical displacement rates calculated in the decomposition of inter-L-SSE periods for the regions Guerrero (**A**) and Oaxaca (**B**). The bottom figures (**C**, **D**, **E** and **F**) shows vertical displacement rates calculated in the decomposition of L-SSE periods for the regions Guerrero (**C** and **D**) and Oaxaca (**E** and **F**) for TT and inter-TT periods. The black vectors are the displacement rates calculated by decomposition. The red vectors are the modeled displacement rates, and the colorbar shows the modeled slip rates at the subduction interface.

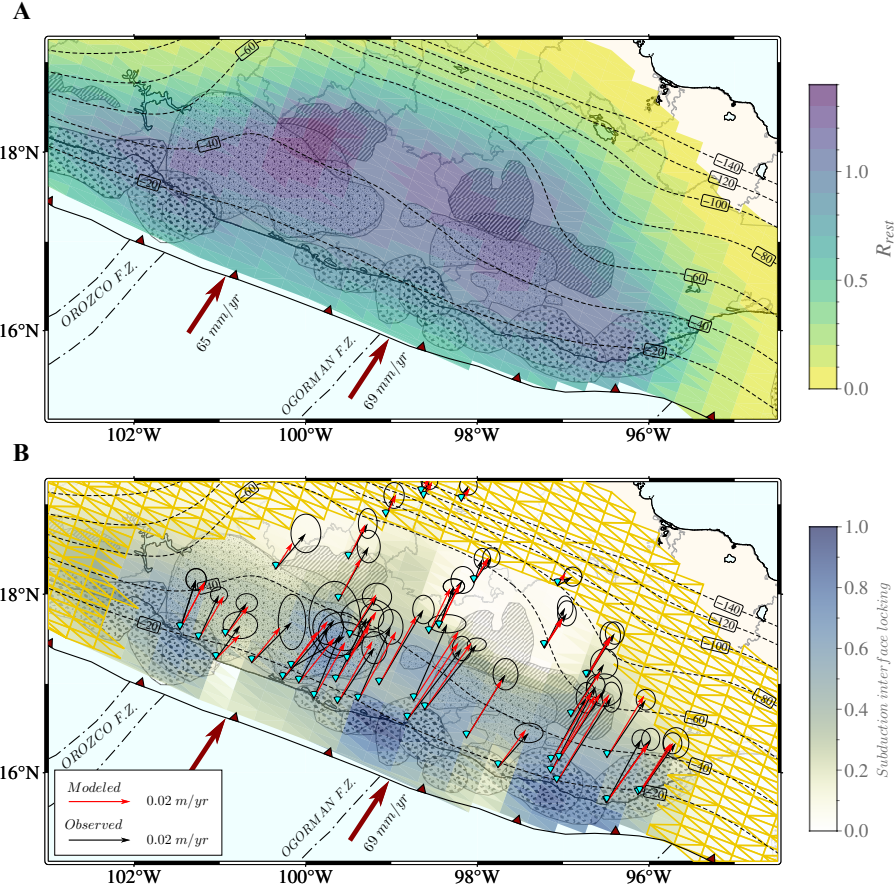


Figure S7: The top map (**A**) displays the restitution index (Eq. (ES5)) calculated for each fault patch for the inter-S-SSE locking model shown in Fig. 6. The bottom figure (**B**) shows the inter-L-SSE locking of the Mexican subduction zone. The black vectors are the inter-L-SSE loading rates calculated by the trajectory model (v in Eq. (ES1)). The red vectors are the modeled surface rates, and the colorbar shows the locking of the subduction interface, calculated as the slip deficit rates divided by the convergence rates. The convergence rates are calculated from the velocity model MORVEL 2010 (DeMets et al., 2010). The dark yellow symbols are showing the patches with a restitution value $R_{rest} \leq 0.6$.

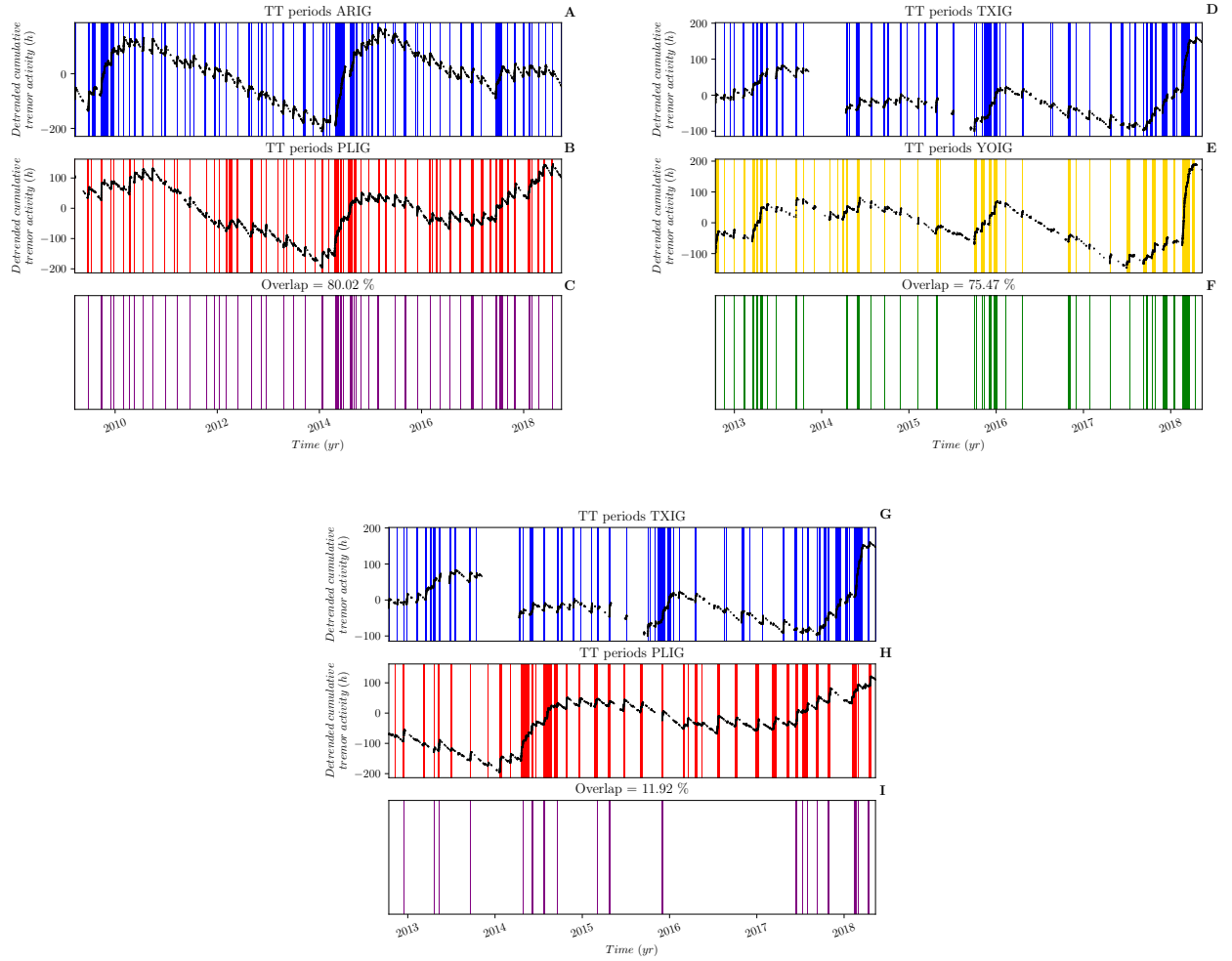


Figure S8: Comparison between Tectonic Tremor bursts detected by two stations in Guerrero (A, B, C), in Oaxaca (D, E, F), and between Guerrero and Oaxaca (G, H, I). In each case, the bottom plots (C, F, I) show the overlapping periods. **A** and **B** are the TT bursts at the seismic stations of ARIG and PLIG (both in Guerrero). **C** are the overlapping TT burst periods between the two seismic stations. **D** and **E** are the TT bursts at the seismic stations of TXIG and YOIG (both in Oaxaca). **F** are the overlapping TT periods between the two seismic stations. **G** and **H** are the TT bursts at the seismic stations of TXIG and PLIG (in Oaxaca and Guerrero respectively). **I** are the overlapping TT burst periods between the two seismic stations.

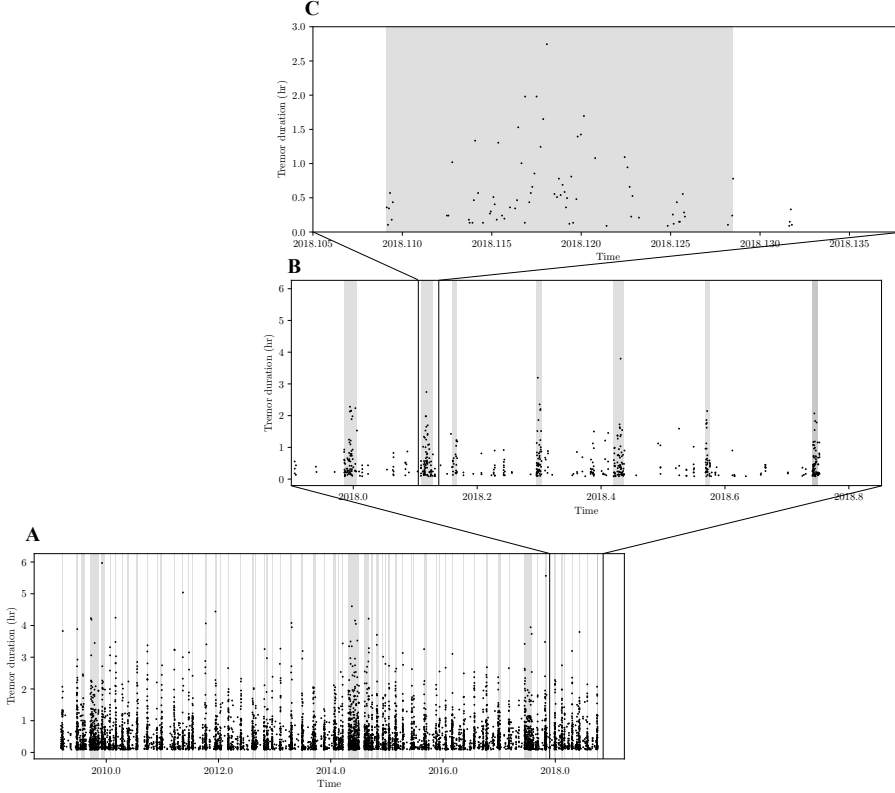


Figure S9: Tremor catalog from [Husker et al. \(2019\)](#) highlighting the tremor clustering visualization at different time scales. **A** Tremor time versus duration for the station ARIG from the catalog by [Husker et al. \(2019\)](#) **B** is a zoom over the year 2018, and **C** is a zoom over an ~ 10 days tremor burst. The grey spans are the bursts detected using our method. The tremor bursts of short duration are not detected by our study, but the major ones are well characterized. The zoom on one single burst (**C**) shows additional complexity that we do not characterize with our tremor catalog..

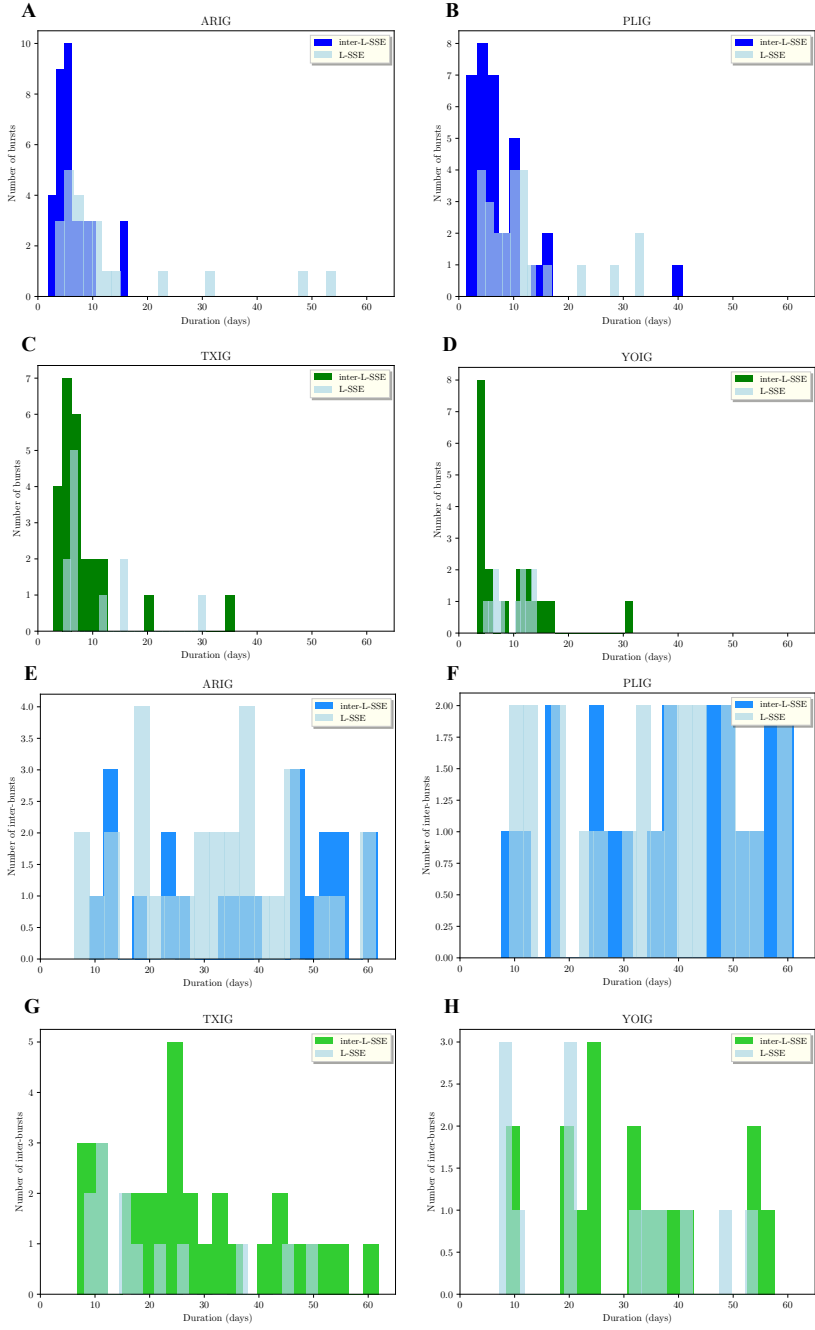


Figure S10: Tremor burst duration histograms. The top 2 histograms (**A** and **B**) show the distribution of tremor burst durations detected for the seismic stations ARIG and PLIG (Fig S7.A,B) in Guerrero. The bursts are sorted based on their occurrence at L-SSE or inter-L-SSE periods. Figures **C** and **D** are histograms for the bursts detected for the stations TXIG and YOIG in Oaxaca (Fig S8.D,E). The histograms (**E**, **F**, **G** and **H**) are the inter-burst durations for the detections at the sites ARIG, PLIG, TXIG and PLIG respectively.

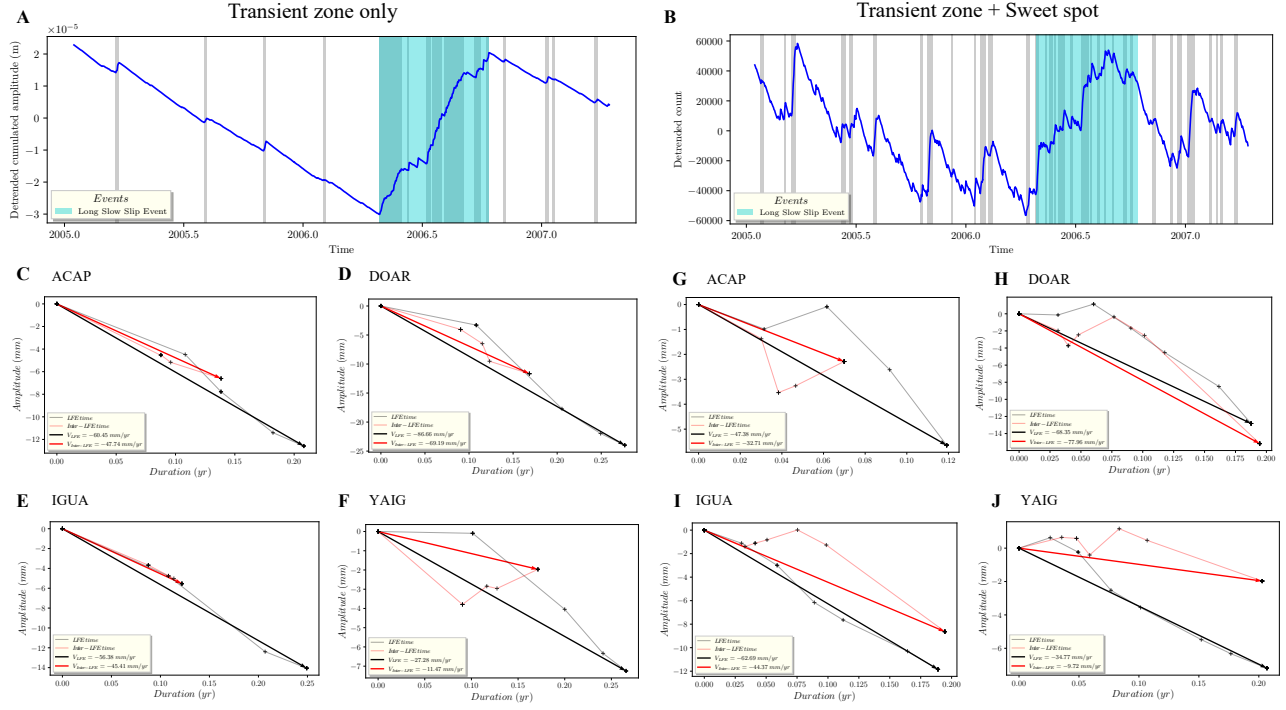


Figure S11: LFE burst analysis and GNSS decomposition. The top left figure **A** shows by the blue curve the detrended cumulated LFE amplitude in the catalog published in Frank and Brodsky (2019), this catalog contains only the LFEs occurring in the transient zone. The grey spans are the detected LFE bursts, and the light blue span is the SSE of 2006 in the Guerrero region. The top right figure **B** shows by the blue curve the detrended count of LFEs in the catalog published by Frank et al. (2014), which contains the LFEs occurring both in the sweet spot and the transient zone. Figures **C,D,E,F** are the decompositions of detrended GNSS data using the LFE bursts defined in figure **A** for the stations ACAP, DOAR, IGUA, and YAIG respectively. The light black lines correspond to offsets during LFE bursts and the light red lines correspond to offsets during inter-LFE periods. Average velocities during LFE bursts and inter-LFE periods are shown by black and red bold arrows respectively. Figures **G,H,I,J** are the resulting decompositions using the LFE bursts defined in **B**.

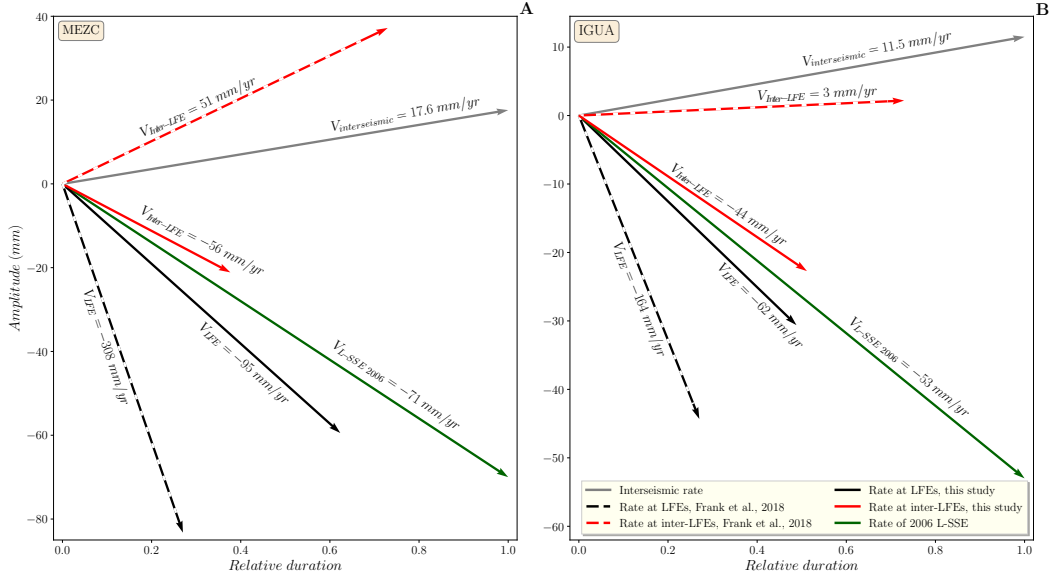


Figure S12: Comparison of decomposed velocities during the L-SSE of 2006. The black arrows are the surface velocities during LFE periods (solid and dashed, for this study and Frank et al., 2018 respectively). The red arrows are the surface velocities in inter-LFE periods (solid and dashed, for this study and Frank et al., 2018 respectively). The dark green arrow is the total average velocity during the L-SSE of 2006. The grey arrows correspond to the inter-seismic velocities calculated using a trajectory model. Note that the duration has been normalized along the x-axis to facilitate the comparison between the two studies.

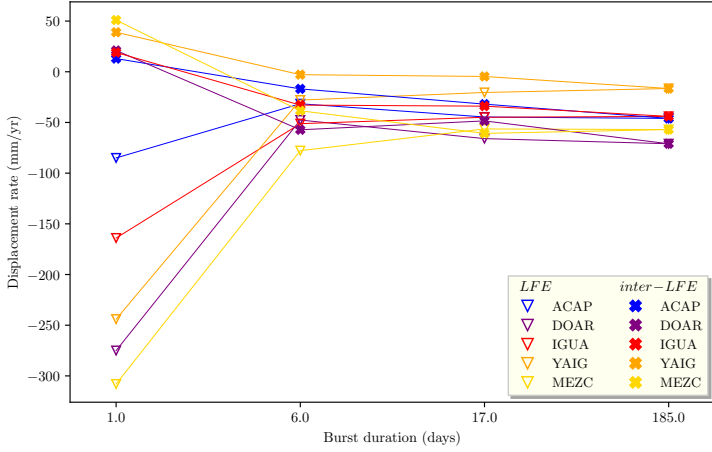


Figure S13: Surface displacement rates as a function of average burst durations. The inverted triangles correspond to surface rates during LFE bursts with added inter-seismic rates, for stations in the Guerrero region: ACAP, DOAR, IGUA, YAIG and MEZC. The crosses are surface rates for inter-LFE periods at the corresponding stations. Four burst average durations are distinguished, the 1 day duration, as defined by Frank et al. (2018), 6 days duration calculated from the LFE catalog by Frank and Shapiro (2014) (containing LFEs from the sweet spot and the transient zone) shown in Fig. S11.B, and a duration of 17 days calculated using from LFE catalog by Frank and Brodsky (2019) (containing only the LFEs from the transient zone) shown in Fig. S11.A. And the total L-SSE period as a burst lasting 185 days. The bursts of average duration of 6 and 17 days were decomposed using our averaging method.

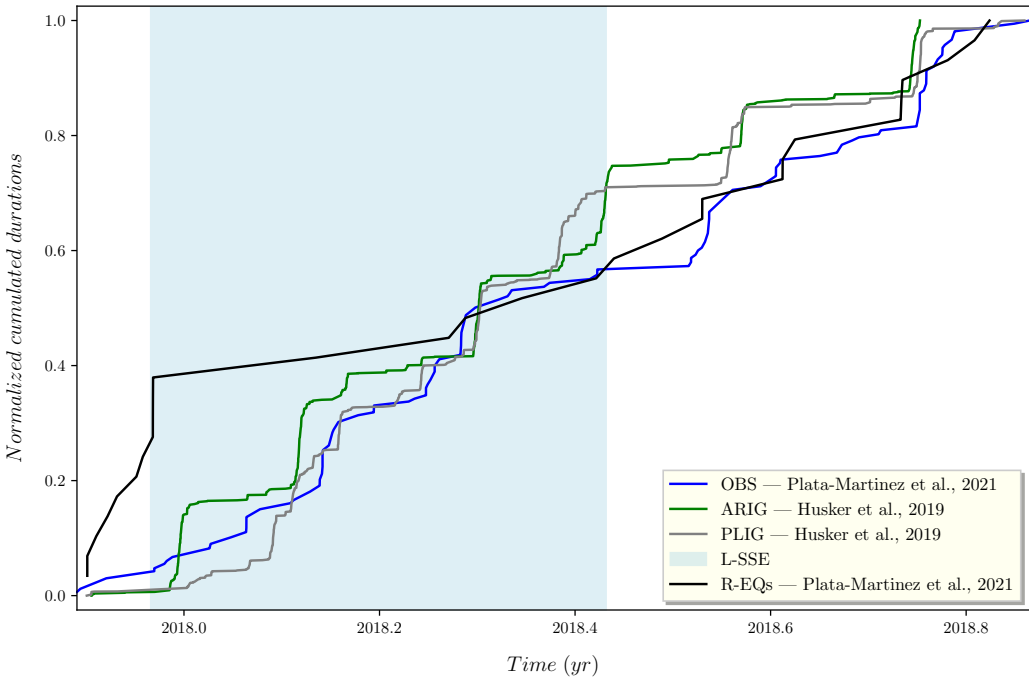


Figure S14: Comparison of shallow and deep tremor activity in the Guerrero region. The green and grey curves are the normalized cumulative tremor durations for the seismic stations ARIG and PLIG respectively (Husker et al., 2019). The blue curve shows the normalized cumulative durations of tremors recorded by OBS (Ocean Bottom Seismometers) in the Guerrero seismic Gap, and the black curve shows the normalized count of repeating earthquakes in the Guerrero Gap, from Plata-Martinez et al. (2021).

Bursts of deep and shallow tremors sometimes occur simultaneously.

3 Supplementary tables

Frank et al. (2015)	Guerrero	Oaxaca
inter-L-SSEs		
LFEs	TTs	TTs
d = 8 days, $M_0 = 8.31e18 \text{ Nm}$	d = 9 days, $M_0 = 6.91 \text{ Nm}$	d = 8 days, $M_0 = 7.68e18 \text{ Nm}$
L-SSEs		
	TTs	TTs
	d = 15 days, $M_0 = 1.64e19 \text{ Nm}$	d = 12 days, $M_0 = 1.13e19 \text{ Nm}$
	inter-TTs	inter-TTs
	d = 29 days, $M_0 = 2.49e19 \text{ Nm}$	d = 22 days $M_0 = 1.75e19 \text{ Nm}$

Table S1: Average moment magnitudes for transient slip events in Mexico. The left column contains the average duration and magnitude for S-SSEs in the Guerrero region, from Frank et al. (2015). The central column is for the Guerrero region, with average duration d and moment magnitudes M_0 for tremor and inter-tremor periods during both L-SSEs and inter-L-SEEs, calculated in this study. The right column is the same but for the Oaxaca region.

Year	Month	Day	Latitude	Longitude	Depth	Magnitude	Duration	Reference
1998	01	01	17.26	-100.11	32.5	6.65	175	Lowry et al. (2001)
2001	10	18	17.27	-100.247	35	7.65	415	Kostoglodov (2003)
2006	02	07	17.26	-100.11	32.5	7.49	349	Radiguet et al. (2011)
2009	06	17	17.55	-100.1	32.5	7.53	434	Radiguet et al. (2012)
2011	11	02	17.93	-99.62	30	5.1	158	
2013	11	09	17.8	-100.5	32.5	7.3	532	Radiguet et al. (2016)
2017	06	04	17.74	-100.15	32.5	6.91	164	Cruz-Atienza et al. (2021)
2017	12	19	17.5	-99.45	32.5	6.93	153	Cruz-Atienza et al. (2021)
2019	02	20	17.85	-100.6	32.5	6.99	310	Cruz-Atienza et al. (2021)
2020	09	15	17.55	-100.1	32.5	6.7	62	
2021	01	14	17.55	-100.1	32.5	6.7	62	

Table S2: L-SSEs catalog in the Guerrero region, adapted from the listed references.

Year	Month	Day	Latitude	Longitude	Depth	Magnitude	Duration	Reference
2004	01	11	16.4	-97.5	30	7.3	131	Graham et al. (2016)
2005	12	24	16.35	-97.5	30	7.1	194	Graham et al. (2016)
2007	02	28	16.2	-97.1	30	6.5	110	Graham et al. (2016)
2008	10	30	16.3	-97.6	37.5	7.2	248	Graham et al. (2016)
2010	12	06	16.25	-97.8	40	7.2	175	Graham et al. (2016)
2012	01	22	16.2	-96.75	30	6.9	58	Graham et al. (2016)
2014	01	11	16.25	-97.5	31	7.1	157	Cruz-Atienza et al. (2021)
2015	10	27	16.25	-97.75	31	7.1	130	Cruz-Atienza et al. (2021)
2017	12	10	17.07	-98.25	31	6.93	67	Cruz-Atienza et al. (2021)
2018	11	22	16.95	-97.71	31	6.92	240	Cruz-Atienza et al. (2021)

Table S3: L-SSEs catalog in the Oaxaca region, adapted from the listed references.

4 Supplementary files

Supp_rates.txt contains the GNSS displacement rates (m/yr) given by GNSS time series decompositions, and the interseismic loading rates calculated with the trajectory model. The file contains the list of stations, and the header describes the content of each column. The first three columns contain the GNSS stations' names, latitudes, and longitudes. The following six columns contain the rates for short-SSEs for the three components (North, East and Vertical), and the corresponding uncertainties (std) for the three components. The twelve following columns contain the rates for long-SSEs for the three components, and the uncertainties, during tremor (trem) and inter-tremor periods (inter). The columns (Inter-Seismic_1) contain the interseismic rates derived from the trajectory model for the three components and their associated uncertainty. The final 6 columns (Inter-Seismic_2) contain inter-tremor loading rates at inter-L-SSE periods.

Bursts_ARIG.txt, **Bursts_PLIG.txt**, **Bursts_TXIG.txt**, **Bursts_YOIG.txt** contain the tremor bursts start and end times for the seismic stations ARIG, PLIG, TXIG and YOIG. The first columns correspond to the start times of the second ones to the end time.

References

- Cruz-Atienza, V.M., Tago, J., Villafuerte, C., Wei, M., Garza-Girón, R., Dominguez, L.A., Kostoglodov, V., Nishimura, T., Franco, S.I., Real, J., Santoyo, M.A., Ito, Y., Kazachkina, E., 2021. Short-term interaction between silent and devastating earthquakes in mexico. *Nature Communications* 12(1), 2172. doi:[10.1038/s41467-021-22326-6](https://doi.org/10.1038/s41467-021-22326-6).
- DeMets, C., Gordon, R.G., Argus, D.F., 2010. Geologically current plate motions. *Geophysical Journal International* 181, 1–80. doi:[10.1111/j.1365-246X.2009.04491.x](https://doi.org/10.1111/j.1365-246X.2009.04491.x).
- Frank, W., Rousset, B., Lasserre, C., Campillo, M., 2018. Revealing the cluster of slow transients behind a large slow slip event. *Science Advances* 4, eaat0661. doi:[10.1126/sciadv.aat0661](https://doi.org/10.1126/sciadv.aat0661).
- Frank, W.B., Brodsky, E.E., 2019. Daily measurement of slow slip from low-frequency earthquakes is consistent with ordinary earthquake scaling. *Science Advances* 5, eaaw9386. doi:[10.1126/sciadv.aaw9386](https://doi.org/10.1126/sciadv.aaw9386).
- Frank, W.B., Radiguet, M., Rousset, B., Shapiro, N.M., Husker, A.L., Kostoglodov, V., Cotte, N., Campillo, M., 2015. Uncovering the geodetic signature of silent slip through repeating earthquakes. *Geophysical Research Letters* 42, 2774– 2779. doi:[10.1002/2015GL063685](https://doi.org/10.1002/2015GL063685).
- Frank, W.B., Shapiro, N.M., 2014. Automatic detection of low-frequency earthquakes (lfes) based on a beamformed network response. *Geophysical Journal International* 197, 1215–1223. doi:[10.1093/gji/ggu058](https://doi.org/10.1093/gji/ggu058).
- Frank, W.B., Shapiro, N.M., Husker, A.L., Kostoglodov, V., Romanenko, A., Campillo, M., 2014. Using systematically characterized low-frequency earthquakes as a fault probe in guerrero, mexico. *Journal of Geophysical Research: Solid Earth* 119, 7686–7700. doi:[10.1002/2014JB011457](https://doi.org/10.1002/2014JB011457).
- Graham, S., DeMets, C., Cabral-Cano, E., Kostoglodov, V., Rousset, B., Walpersdorf, A., Cotte, N., Lasserre, C., McCaffrey, R., Salazar-Tlaczani, L., 2016. Slow slip history for the mexico subduction zone: 2005 through 2011. *Pure and Applied Geophysics* 173, 3445–3465. doi:[10.1007/s00024-015-1211-x](https://doi.org/10.1007/s00024-015-1211-x).
- Husker, A., Frank, W.B., Gonzalez, G., Avila, L., Kostoglodov, V., Kazachkina, E., 2019. Characteristic tectonic tremor activity observed over multiple slow slip cycles in the mexican subduction zone. *Journal of Geophysical Research: Solid Earth* 124, 599–608. doi:[10.1029/2018JB016517](https://doi.org/10.1029/2018JB016517).

- Kostoglodov, V., 2003. A large silent earthquake in the guerrero seismic gap, mexico. *Geophysical Research Letters* 30(15), 1807. doi:[10.1029/2003gl017219](https://doi.org/10.1029/2003gl017219).
- Lowry, A.R., Larson, K.M., Kostoglodov, V., Bilham, R., 2001. Transient fault slip in guerrero, southern mexico. *Geophysical Research Letters* 28(19), 3753–3756. doi:[10.1029/2001gl013238](https://doi.org/10.1029/2001gl013238).
- Marill, L., Marsan, D., Socquet, A., Radiguet, M., Cotte, N., Rousset, B., 2021. 14-year acceleration along the japan trench and the sagami trough. *Earth and Space Science Open Archive* doi:[10.1002/essoar.10504635.1](https://doi.org/10.1002/essoar.10504635.1).
- Okada, Y., 1985. Surface deformation due to shear and tensile faults in a half-space. *Bulletin of the Seismological Society of America* 75(4), 1135–1154. doi:[10.1785/BSSA0750041135](https://doi.org/10.1785/BSSA0750041135).
- Plata-Martinez, R., Ide, S., Shinohara, M., Garcia, E.S., Mizuno, N., Dominguez, L.A., Taira, T., Yamashita, Y., Toh, A., Yamada, T., Real, J., Husker, A., Cruz-Atienza, V.M., Ito, Y., 2021. Shallow slow earthquakes to decipher future catastrophic earthquakes in the guerrero seismic gap. *Nature Communications* 12, 3976. doi:[10.1038/s41467-021-24210-9](https://doi.org/10.1038/s41467-021-24210-9).
- Radiguet, M., Cotton, F., Vergnolle, M., Campillo, M., Valette, B., Kostoglodov, V., Cotte, N., 2011. Spatial and temporal evolution of a long term slow slip event: the 2006 guerrero slow slip event. *Journal of Geophysical Research: Solid Earth* 184(2), 816–828. doi:[10.1111/j.1365-246x.2010.04866.x](https://doi.org/10.1111/j.1365-246x.2010.04866.x).
- Radiguet, M., Cotton, F., Vergnolle, M., Campillo, M., Walpersdorf, A., Cotte, N., Kostoglodov, V., 2012. Slow slip events and strain accumulation in the guerrero gap, mexico. *Journal of Geophysical Research* 117(B4). doi:[10.1029/2011jb008801](https://doi.org/10.1029/2011jb008801).
- Radiguet, M., Perfettini, H., Cotte, N., Gualandi, A., Valette, B., Kostoglodov, V., Lhomme, T., Walpersdorf, A., Cabral Cano, E., Campillo, M., 2016. Triggering of the 2014 mw7.3 papanoa earthquake by a slow slip event in guerrero, mexico. *Nature Geoscience* 9, 829–833. doi:[10.1038/ngeo2817](https://doi.org/10.1038/ngeo2817).
- Tarantola, A., 2005. Inverse Problem Theory and Methods for Model Parameter Estimation. Society for Industrial and Applied Mathematics. doi:[10.1137/1.9780898717921](https://doi.org/10.1137/1.9780898717921).